

# Open Rotor Computational Aeroacoustic Analysis with an Immersed Boundary Method

Christoph Brehm<sup>\*1</sup>

<sup>1</sup>*Science and Technology Corporation, Moffett Field, CA 94035*

Michael F. Barad<sup>\*2</sup>, and Cetin C. Kiris<sup>†2</sup>

<sup>2</sup>*NASA Ames Research Center, Moffett Field, CA 94035*

Reliable noise prediction capabilities are essential to enable novel fuel efficient open rotor designs that can meet the community and cabin noise standards. Toward this end, immersed boundary methods have reached a level of maturity where more and more complex flow problems can be tackled with this approach. This paper demonstrates that our higher-order immersed boundary method provides the ability for aeroacoustic analysis of wake-dominated flow fields generated by a contra-rotating open rotor. This is the first of a kind aeroacoustic simulation of an open rotor propulsion system employing an immersed boundary method. In addition to discussing the methodologies of how to apply the immersed boundary method to this moving boundary problem, we will provide a detailed validation of the aeroacoustic analysis approach employing the Launch Ascent and Vehicle Aerodynamics (LAVA) solver. Two free-stream Mach numbers with  $M=0.2$  and  $M=0.78$  are considered in this analysis that are based on the nominally take-off and cruise flow conditions. The simulation data is compared to available experimental data and other computational results employing more conventional CFD methods. Spectral analysis is used to determine the dominant wave propagation pattern in the acoustic near-field.

## I. Introduction

There has been a renewed interest in pursuing contra-rotating open rotor (CROR) propulsion technology due to the large potential of significantly reducing fuel consumption. A main concern for the design of such systems is that they must meet community noise and cabin noise standards. Hence, providing reliable noise prediction capabilities for contra-rotating open rotors is essential in the design of low-noise rotor propulsion systems. In recent years, NASA initiated several research efforts that have assessed the capabilities on noise source prediction and analysis of contra-rotating open rotors. Several low to high fidelity simulation tools were used to provide noise predictions and their results were compared to experimental data.<sup>1-5</sup> One of the key challenges is to conduct efficient high-fidelity simulations of the contra-rotating open rotor system including installation effects.

In order to simulate the flow around the contra-rotating open rotor the Cartesian AMR solver module within the Launch Ascent and Vehicle Aerodynamics (LAVA) framework is utilized. To obtain the noise signature in the far-field, the highly unsteady flow field in the source region is simulated with an implicit large-eddy simulation approach combined with the Ffowcs-Williams and Hawkings (FW-H) method for acoustic noise propagation away from the source region. The non-conventional immersed boundary approach presented here is accompanied with a parallel effort utilizing LAVA's curvilinear-overset approach as presented in the companion paper by Housman and Kiris.<sup>6</sup> While utilizing the current simulation results to conduct an acoustic analysis of the acoustic near field, a key objective of this paper is to simulate this highly complex flow field by employing a higher-order accurate immersed boundary method and validate this approach against experimental data. This is the first ever application of an immersed boundary method for noise prediction of an open rotor system. It will be demonstrated that LAVA-Cartesian provides a reliable noise prediction capability that can then be used to also study installation effects.

---

<sup>\*</sup>Research Scientist, Computational Aerosciences Branch, NAS Division, MS N258-2 and AIAA Senior Member

<sup>†</sup>Branch Chief, Computational Aerosciences Branch, NAS Division, MS N258-2 and AIAA Senior Member

Immersed Boundary Methods (IBMs) have been developed for many years and have appeared in various forms since they were first introduced by Peskin<sup>7,8</sup> (see for example Goldstein *et al.*,<sup>9</sup> LeVeque and Li,<sup>10</sup> Wiegmann and Bube,<sup>11</sup> Linnick and Fasel,<sup>12</sup> Johansen and Collela,<sup>13</sup> Mittal and Iaccarino,<sup>14</sup> Zhong,<sup>15</sup> Duan *et al.*<sup>16</sup> and many others). These methods were first introduced as a nontraditional approach for numerically solving initial/boundary-value problems for complex geometries on Cartesian meshes and have matured to become increasingly important for a wide range of applications.<sup>17–19</sup> One of the key advantages of immersed boundary methods is that the computational meshes can be automatically generated starting from a water tight surface triangulation independent of the complexity of the geometry. The grid-generation process for body-fitted structured or unstructured grids for complex geometries is generally very laborious because the process aims at generating well behaved grids that have sufficient local resolution while minimizing the total number of required grid points. Except for simple geometries, these conflicting requirements can lead to a deterioration in grid quality, thereby negatively impacting the accuracy and convergence properties of the flow solver. For highly complex geometries, which are relevant for many fields of science and engineering, the process of generating a high-quality grid is extremely time consuming. For flows involving moving and deforming boundaries, IBMs also provide clear advantages over classical body-fitted grid approaches. Simulating such flows on body-fitted grids requires generating a new grid at each time step and a procedure to project the solution onto this new grid. These two characteristics (grid deformation and projection of solution) for body-fitted grids associated with simulating flows with moving and deforming boundaries may negatively impact the accuracy, robustness, and computational cost of the numerical solution method. Particularly, in cases where the boundary exhibits large relative motions, body-conformal grid strategies cause immense difficulties in the solution procedure. This is where an immersed boundary method with its fully Eulerian approach provides great advantages. IBMs provide a much more convenient way of including the body motion and deformation by using a stationary non-deforming Cartesian grid. While these methods simplify the grid generation process, a detailed mathematical understanding of the IBM is necessary to avoid a negative impact of the boundary treatment on the robustness, the convergence behavior and the accuracy of the numerical scheme.

Immersed boundary methods also possess well known shortcomings that have limited their applicability to a wider range of applications. At high Reynolds numbers the immersed boundary method becomes inefficient because it generally utilizes Cartesian grid cells to resolve thin boundary layers, while conventional body-fitted grid approaches rely on high aspect ratio cells in the vicinity of the wall. Most IBMs are also only lower-order accurate and suffer from robustness issues when extended to higher-order. The near wall accuracy is, however, critical when simulating laminar to turbulent transition scenarios for wall-bounded flows to capture relevant instability mechanisms. Higher-order immersed boundary methods have been presented in a number of research studies by Linnick and Fasel,<sup>12</sup> Zhong,<sup>15</sup> Duan *et al.*,<sup>16</sup> Brehm and Fasel,<sup>20</sup> Brehm *et al.*,<sup>21</sup> and others. The current method employed within NASA’s LAVA CFD solver<sup>17</sup> is based on the higher-order immersed boundary method discussed in Brehm *et al.*<sup>21</sup>

The current paper is organized as follows: Section II introduces LAVA and the numerical scheme used to solve the compressible Navier-Stokes equations. Section III provides an overview of the simulation setup, such as the geometry and computational mesh used in the simulation. Section IV presents an unsteady flow visualization displaying some of the flow features of the low and high speed cases. A comparison of the present CFD data obtained on different grids with available experimental PIV and acoustic data is given in Section V. The simulation data is utilized to conduct a brief acoustic analysis of the pressure field in the near field employing spectral analysis in Section VI. The last Section VII summarizes some of the key findings of the paper and presents some future directions of the ongoing research.

## II. Numerical Methods

### II.A. Interior Spatial and Temporal Discretizations

In this work, the compressible Navier-Stokes equations are solved in conservative form considering an ideal, Newtonian, non-reactive gas. The governing equations can be written in vector form as follows

$$\frac{\partial \mathbf{W}}{\partial t} + \nabla \cdot (\vec{\mathcal{F}} - \vec{\mathcal{F}}_v) = 0, \quad \text{with } \vec{\mathcal{F}} = (\mathbf{F}^1, \mathbf{F}^2, \mathbf{F}^3) \quad \text{and} \quad \vec{\mathcal{F}}_v = (\mathbf{F}_v^1, \mathbf{F}_v^2, \mathbf{F}_v^3). \quad (1)$$

The conservative variable vector  $\mathbf{W} = (\rho, \rho u, \rho v, \rho w, \rho H - p)^T$  and the inviscid fluxes are

$$\mathbf{F}^1 = \begin{bmatrix} \rho u \\ \rho u^2 + p \\ \rho uv \\ \rho uw \\ \rho uH \end{bmatrix}, \mathbf{F}^2 = \begin{bmatrix} \rho v \\ \rho vu \\ \rho v^2 + p \\ \rho vw \\ \rho vH \end{bmatrix}, \text{ and } \mathbf{F}^3 = \begin{bmatrix} \rho w \\ \rho wu \\ \rho wv \\ \rho w^2 + p \\ \rho wH \end{bmatrix},$$

where the total enthalpy is  $H = h + \vec{u} \cdot \vec{u}/2$ . The viscous fluxes are

$$\mathbf{F}_v^1 = \begin{bmatrix} 0 \\ \tau_{xx} \\ \tau_{xy} \\ \tau_{xz} \\ f_v^1 \end{bmatrix}, \mathbf{F}_v^2 = \begin{bmatrix} 0 \\ \tau_{yx} \\ \tau_{yy} \\ \tau_{yz} \\ f_v^2 \end{bmatrix}, \text{ and } \mathbf{F}_v^3 = \begin{bmatrix} 0 \\ \tau_{zx} \\ \tau_{zy} \\ \tau_{zz} \\ f_v^3 \end{bmatrix}.$$

In the above equations  $\rho$  is the density,  $\mathbf{u} = (u, v, w)$  is the velocity vector,  $\underline{\delta}$  is the unit tensor,  $p$  is the static pressure,  $T$  is the temperature,  $E$  is the total energy,  $\gamma$  is the specific heat ratio,  $R$  is the gas constant, and  $\kappa$  is the thermal conductivity. The total energy, ideal gas law, and viscous stress tensor are defined as

$$E = \frac{p}{\gamma - 1} + \frac{1}{2}\rho\mathbf{u} \cdot \mathbf{u}, \quad p = \rho RT, \quad \text{and} \quad \boldsymbol{\tau} = \mu(2\underline{\mathbf{S}}) + \left(\beta - \frac{2}{3}\mu\right)(\nabla \cdot \mathbf{u})\underline{\delta}. \quad (2a)$$

The dynamic viscosity is given by  $\mu$ ,  $\beta$  is the bulk viscosity, and the strain rate tensor  $\underline{\mathbf{S}}$  is defined as  $\underline{\mathbf{S}} = \frac{1}{2}(\nabla\mathbf{u} + (\nabla\mathbf{u})^T)$ .

## II.B. LAVA-Cartesian AMR Solver

The computational framework, called Launch Ascent and Vehicle Aerodynamics (LAVA), is essentially grid agnostic by providing the capability of being able to solve the compressible Navier-Stokes equations on block-structured Cartesian, curvilinear-overset, and unstructured polyhedral grids. For each grid type a different solver module is utilized that are referred to as LAVA-Cartesian, LAVA-Curvilinear, and LAVA-Unstructured. While the long term objective is to provide a common communication interface between all three solver modules, currently only LAVA-Cartesian and LAVA-Unstructured are fully coupled. LAVA provides additional modules for acoustic far-field propagation and scattering, conjugate heat transfer, and computational structural dynamics. In the present paper, LAVA-Cartesian is used together with the Ffowcs-Williams Hawkins (FW-H) method for acoustic far-field propagation.

LAVA-Cartesian is a block-structured, Immersed Boundary (IB) AMR code. This methodology is capable of automatically generating, refining, and coarsening nested Cartesian volumes. LAVA's AMR-IB method is designed to automatically generate the volume grids from a closed surface triangulation, and dynamically track important flow features as they develop. AMR is a proven methodology for multi-scale problems with an extensive existing mathematical and software knowledge base.<sup>22-26</sup> The code has been extended using data structures and inter-level operators from the high-performance Chombo AMR library<sup>27</sup> to provide a multi-resolution capability that can coarsen and refine the grid locally as a simulation progresses. To account for flow discontinuities, a sixth-order accurate shock-capturing WENO scheme is utilized. The characteristic variable transformation is applied to a Rusanov-type flux vector splitting scheme. The accuracy and computational efficiency of the higher-order shock capturing schemes of the current solver has been previously analyzed in Brehm *et al.*<sup>21</sup> The viscous terms are discretized with fourth-order accuracy. The fourth-order accurate explicit Runge-Kutta scheme is used for time-integration. LAVA-Cartesian and LAVA's FW-H solver have previously been validated for aero-acoustic simulations of different types of jet impingement flows.<sup>28, 29</sup>

## II.C. Immersed Boundary Method

In this section, the theoretical basis of the IBM presented in Brehm and Fasel<sup>20</sup> and its extension to the compressible Navier-Stokes equations are briefly outlined. Many immersed methods have been developed in

the past; however, in the derivation of these schemes, usually only the order of the local truncation error or accuracy of the numerical scheme has been considered. *A posteriori*, the numerical stability of these schemes is commonly demonstrated (in a global sense) by considering a number of different test-problems, and in a few cases, an additional global matrix stability analysis is employed (see for example Zhong<sup>15</sup>). The basis of the IBM by Brehm and Fasel<sup>20</sup> is that the stencil coefficients are locally optimized in order to improve the stability of the scheme.

The notion of developing a strategy for improving the spectral properties of immersed methods originated from the idea that the stability of the numerical scheme can be formulated as an  $N$ -dimensional optimization problem, where  $N$  represents the number of irregular grid points. Instead of solely considering the local truncation error in the derivation of the finite-difference grid stencil at an irregular grid point, an over-determined system of equations is constructed to determine the stencil coefficients. An over-determined system of equations is employed because it allows to select free parameters, which can be tuned towards optimizing the stability properties of the finite-difference scheme. Figure 1a illustrates the dependence of the spectral radius for the discretization matrix of a 1D advection-diffusion equation on the free stencil coefficient  $\tilde{\alpha}_1$  for two boundary distances  $\psi = 0.1$  and  $\psi = 0.9$ . An optimal value for  $\tilde{\alpha}_1$  can be chosen to create a stable immersed boundary scheme. Assuming one free parameter per irregular grid point an  $N$ -dimensional optimization problem for  $N$  irregular grid points is obtained. Figure 1b provides an overview of the irregular point layout around a circle immersed into a Cartesian mesh for a third-order accurate immersed boundary scheme.

The objective function of the optimization problem must be carefully chosen and depends on the nature of the particular partial-differential equation of interest. For advection-diffusion-type equations, the spectral radius of the update matrix may be considered an appropriate objective function. In the current paper, we refer to the update matrix as the matrix which updates the solution from time  $t_n$  to the next time-step,  $t_{n+1}$ . The update matrix, therefore, contains information about the spatial and temporal discretization of the numerical scheme. The spectral radius is well-suited in this situation, because its actual value is associated with the stability of the numerical scheme and it can be used to formulate a necessary condition for the stability of the update matrix. For non-linear systems of equations, a linearization is necessary prior to applying the outlined linear stability analysis concepts. The immersed boundary method used in this paper solely uses linear stability theory and, therefore, neglects possible non-linear effects on the stability.

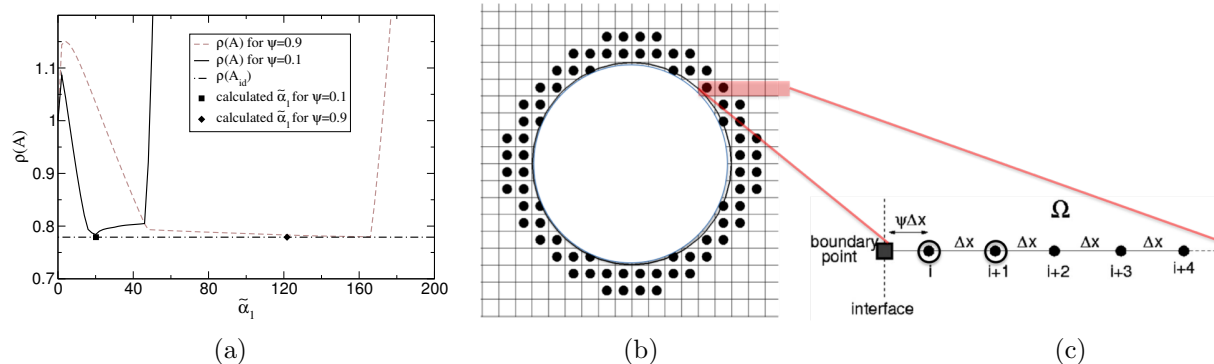


Figure 1. (a) Dependence of spectral radius on free stencil coefficient  $\tilde{\alpha}_1$ . (b) Localization illustrated in 2D for circle immersed into Cartesian grid. (c) Computational setup in the vicinity of the immersed boundary including irregular grid points ( $\odot$ ), point in fluid ( $\bullet$ ) and point in solid (dropped) ( $\circ$ ) the computational domain, and a boundary point ( $\blacksquare$ ).

In principle, it is possible to solve a coupled  $N$ -dimensional optimization problem for  $N$  irregular grid points. From a practical point of view, however, it is not very efficient or desirable to solve such a large system of equations, especially for fluid-structure interaction (FSI) problems where the grid topology is time dependent, thereby requiring this procedure to be repeated at each time-step. Therefore, as schematically shown in Figures 1b and 1c we aim at isolating the boundary stencils from the remainder of the computational domain so that the optimization problem can be formulated for each irregular grid-point separately. Instead of solving a global  $N$ -dimensional optimization problem we solve 1D optimization problems at each of the  $N$  irregular grid point individually. This approach greatly reduces the computational effort needed to determine the “optimal” stencil coefficients. We refer to the aspect of turning the global  $N$ -dimensional problem into  $N$  one-dimensional problems as “localization” or “localization assumption”. In Brehm and Fasel,<sup>20</sup> it was

demonstrated, both numerically and analytically, that for advection-diffusion type equations, the localization assumption appears to be valid as long as the von Neumann number does not reach a limiting value. In the following discussion, the basic steps for extending the IBM for the compressible Navier-Stokes equations are outlined.

The main difference for the application of the IBM to the compressible Navier-Stokes equations instead of the incompressible Navier-Stokes equations (solved by utilizing the approximate projection method) is the use of numerical fluxes. Flux vector splitting schemes, i.e. van Leer,<sup>30</sup> Rusanov, and AUSMPW+, are adopted here. In the flux vector splitting approach, the convective flux is divided into a forward-flux and a backward-flux,  $\mathbf{F} = \mathbf{F}^- + \mathbf{F}^+$ . The flux vector splitting approach is also applied at irregular grid points, which can be employed to stabilize the irregular grid stencils. Assuming subsonic flow speeds in the vicinity of the immersed boundary, upwinding can always be applied in the upwind direction towards the wall. This is in contrast to the scalar advection equation where the advection speed determines the upwind direction. The basic ideas of the IBM implementation are discussed for the 1D Euler equations in conservative variable formulation,

$$\begin{pmatrix} \rho \\ \rho u \\ E \end{pmatrix}_t = \begin{pmatrix} \rho u \\ \rho u^2 + p \\ u(E + p) \end{pmatrix}_x, \quad (3)$$

where the total energy can be expressed as  $E = \rho(T/((\gamma - 1)\gamma M^2) + u^2/2)$ . The fluid is assumed to be an ideal gas, which can be modeled by the equation of state. Applying the flux vector splitting approach to the 1D Euler equations leads to

$$\mathbf{W}_t = \mathbf{F}_x = \mathbf{F}_x^- + \mathbf{F}_x^+, \quad (4)$$

where the solution vector can be written as  $\mathbf{W} = (w_1, w_2, w_3)^T = (\rho, \rho u, E)^T$ . In order to numerically analyze the 1D Euler system in Equation (4), the Jacobian,  $\partial\mathbf{F}/\partial\mathbf{W}$ , is introduced,

$$\mathbf{W}_t = \frac{\partial\mathbf{F}}{\partial\mathbf{W}} \cdot \frac{\partial\mathbf{W}}{\partial x} = \frac{\partial\mathbf{F}^-}{\partial\mathbf{W}} \cdot \frac{\partial\mathbf{W}}{\partial x} + \frac{\partial\mathbf{F}^+}{\partial\mathbf{W}} \cdot \frac{\partial\mathbf{W}}{\partial x}. \quad (5)$$

This leads to an equation including the derivatives of the forward/backward-flux vectors,  $\mathbf{F}^\pm$ , with respect to the solution vector  $\mathbf{W}$ . The gradient of the convective flux vectors,  $\mathbf{F}^\pm$ , is discretized with the discrete forward difference operator,  $\underline{\mathbf{D}}_x^+$ , (for the forward-flux) and in backward direction with the discrete backward difference operator,  $\underline{\mathbf{D}}_x^-$ , (for the backward-flux),

$$\begin{aligned} \mathbf{W}_t &= \frac{\partial\mathbf{F}^+}{\partial\mathbf{W}} \cdot \frac{\partial\mathbf{W}}{\partial x} + \frac{\partial\mathbf{F}^-}{\partial\mathbf{W}} \cdot \frac{\partial\mathbf{W}}{\partial x} \\ &\cong \frac{\partial\mathbf{F}^+}{\partial\mathbf{W}} \cdot (\underline{\mathbf{D}}_x^+ \cdot \mathbf{W}) + \frac{\partial\mathbf{F}^-}{\partial\mathbf{W}} \cdot (\underline{\mathbf{D}}_x^- \cdot \mathbf{W}). \end{aligned} \quad (6)$$

difference operators,  $\underline{\mathbf{D}}_x^\pm$ , are provided in Brehm *et al.*<sup>21</sup> For an irregular grid point with an immersed boundary located to the left, the optimization procedure is only applied to the differentiation of the forward flux and to the differentiation of the backward flux when the immersed boundary located to the right. The  $n^{\text{th}}$ -order accurate finite difference operator for the differentiation of the backward flux is obtained by utilizing  $n + 2$  grid points (including the boundary point) and applying a least-squares procedure to determine the stencil coefficients for the over-determined system of equations. In order to obtain pressure and temperature boundary conditions a weighted-least-squares interpolation approach is utilized. For slip wall boundary conditions the velocity field is also extrapolated towards the grid line intersection points while imposing the no-penetration condition ( $\mathbf{v} \cdot \mathbf{n} = 0$ ) at boundary. More details about the basics of the immersed boundary method can be found in Brehm *et al.*<sup>20,21</sup>

Some of the key challenges for simulating the contra-rotating open rotor system is the treatment of the thin rotor blades, accounting for the thin boundary layer near the blades, and dealing with the moving boundary. The companion paper by Brehm *et al.*<sup>31</sup> provides a more detailed discussion of how to deal with these challenges. The treatment of the thin rotor blades only effects the cloud selection process for the boundary condition extrapolation stencil since the current sharp immersed boundary method does not utilize ghost cells. The algorithm ensures that only points are selected for the point cloud if they reside on the same side of the boundary as the irregular grid point. To incorporate the effect of the thin boundary layers a partial slip approach was chosen. This partial slip approach was first successfully used to simulate

the flow around the partially dressed landing gear for the AIAA Workshop on Benchmark problems for Airframe Noise Computations (BANC). A detailed discussion of this approach will be presented in Brehm *et al.*<sup>32</sup> There are two additional challenges that had to be addressed in particular for moving geometries: (1) speeding up the geometry queries and regeneration of irregular stencils after moving the geometry and (2) the treatment of Freshly Cleared Cells (FCC). Parallel geometry kernels were implemented to allow fast inside-outside (in-out) testing and exact computation of the distance from the irregular grid points to the surface triangulation (including point to plane and point to edge cases). An x-ray algorithm employing multi-resolution binning is used for in-out testing and a modified KD-tree search algorithm for the minimum distance calculation. Since the FCCs do not contain a valid time history their state vector is initialized considering valid grid points (not including other FCC) in the neighborhood of the FCC.

### III. Simulation Setup

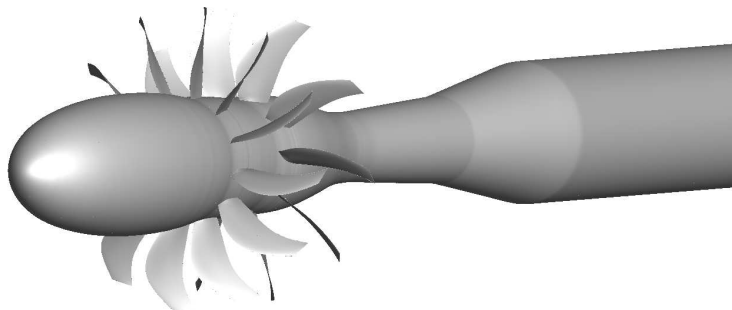


Figure 2. Uninstalled contra-rotating open rotor geometry used in the present CFD analysis.

Figure 2 presents the contra-rotating open rotor geometry used in the present CFD simulations. The CROR blade set shown in Figure 2 is a relatively modern GE design, namely F31/A31, with 12 blades on the front rotor and 10 blades on the second rotor. The front and aft rotor diameters are 0.66m and 0.63m, respectively. The two rotors are separated by a distance of 0.2m. Different nominal blade setting angles for the front and aft rotors were used for the low and high Mach number cases considered in this paper. For the high speed case at Mach 0.78, the blade setting angles are  $64.4^\circ$  and  $61.8^\circ$  and for the nominal take-off condition at Mach 0.2, the blade setting angles are  $40.1^\circ$  and  $40.8^\circ$ . The blade setting angles are measured at 75% radius. The simulated RPMs for the high speed case are 6848/6848 and 6303/6303 for the low speed case. The simulation results are compared to two experimental data sets. The high-speed aerodynamics and acoustic data were obtained for a model scale geometry in NASA’s 8-foot  $\times$  6-foot wind tunnel at cruise conditions at Mach 0.78. The low Mach number case was tested in NASA’s 9-foot  $\times$  15-foot low-speed acoustic wind tunnel. The aerodynamic and acoustic data were acquired for the rotors in uninstalled configuration without fuselage and pylon at zero angle of attack.

Cases	Low Speed (Nominal Take-Off)	High Speed (Cruise)
Mach	0.20	0.78
Rotation speed [RPM]	6303	6848
Pressure [Pa]	101,325	101,325
Temperature [K]	288.15	288.15
Velocity [m/s]	(68.1,0,0)	(265.5,0,0)
Blade setting (fwd/aft)[ $^\circ$ ]	40.1/40.8	64.4/61.8
Radial distances of Kulite sensors [m]	1.524	0.43, 0.51, 0.69, 0.87, 1.16
Geometry details	No wind-tunnel geometry included	No wind-tunnel geometry included, but plate effect studied

Table 1. Low and high speed simulation details.

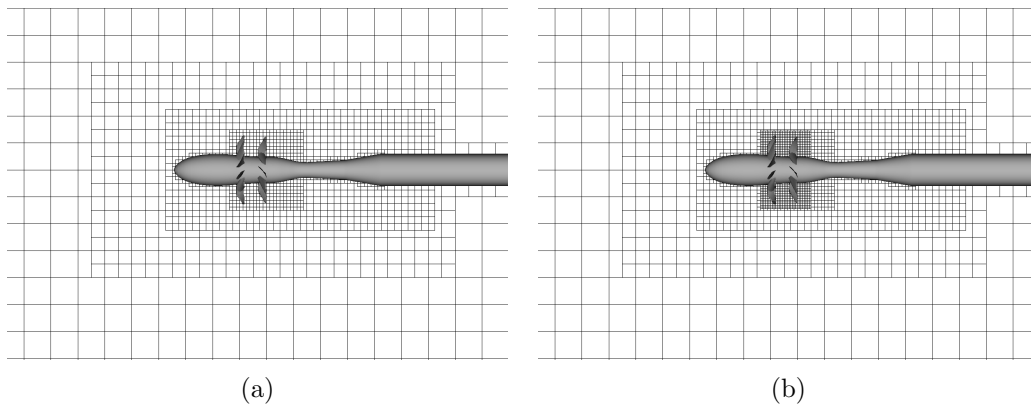


Figure 3. Computational mesh layout in the vicinity of the open rotor geometry for the (a) coarse and (b) fine grids.

A cut through the computational mesh employed for the current simulations is shown in Figures 3a and 3b for the coarse and fine grids. Two computational meshes are utilized with 150 and 500 million grid points to test the sensitivity of the simulation results with respect to the grid resolution. Each Cartesian box shown in Figures 3a and 3b contains  $16^3$  grid points. Grid refinement is applied around the front and rear rotors, and the wake, where high unsteadiness and large gradients are expected. Since storing the entire volume data for each time-step requires excessive large memory, several sampling planes were used to gather the unsteady flow data at each time-step. The unsteady flow analysis was applied to the data recorded in these sampling planes. Note that as indicated throughout this paper flow quantities were normalized with the free stream flow quantities, i.e., free-stream velocity,  $V_\infty$ , pressure,  $p_\infty$ , and temperature,  $T_\infty$ . The Reynolds number based on blade diameter  $D$ ,  $V_\infty$ , and  $T_\infty$  is approximately  $1.2 \times 10^7$  for the free-stream Mach number 0.78 and  $0.3 \times 10^7$  for the free-stream Mach number 0.2.

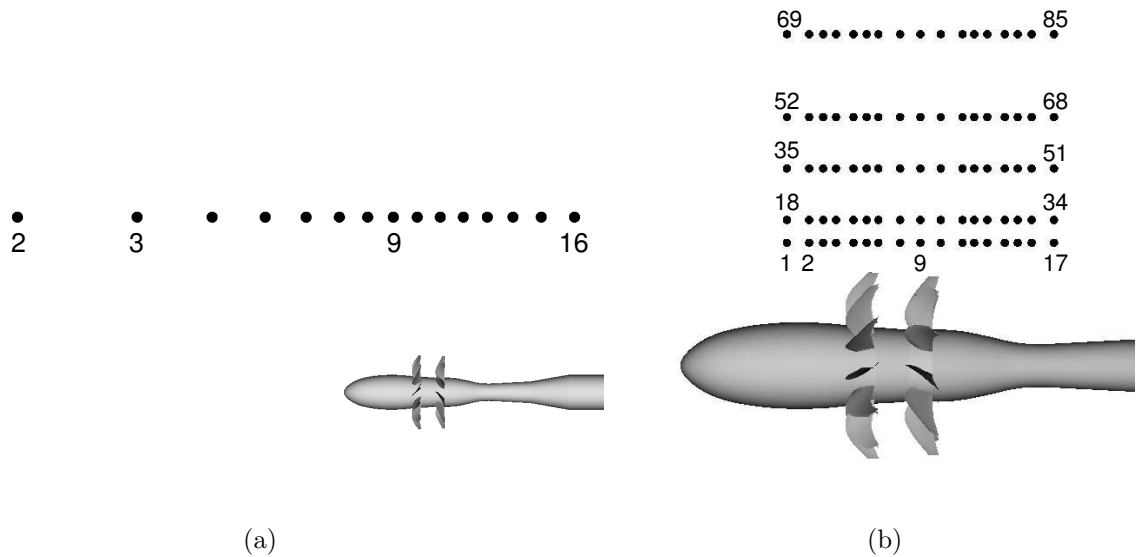


Figure 4. Kulite sensor locations for (a) low and (b) high speed measurements.

In the experiments the acoustic data were obtained at discrete locations in the far-field. The black dots in Figures 4a and 4b mark the Kulite sensor locations where experimental data is available. The Kulite sensor locations are distributed very differently for the low and high speed experiments that were conducted in separate wind tunnels. For the simulation of the high-speed test, the grid resolution is sufficient to resolve acoustic waves associated with the fundamental frequencies of the front and rear rotors for all Kulite sensors shown in Figure 4b without introducing too much numerical dissipation. The first and last rows are roughly 1 and 4 wavelengths away from the rotor axis based on the average wavelength of the blade-passing frequency of the front (BPF1) and rear rotors (BPF2). For the simulation of the low-speed test, the acoustic signal

is sufficiently resolved between sensors 8 and 12. For the other point probes the Ffowcs-Williams Hawkins (FW-H) method is used to propagate the sound signature from the near-field to the far-field sound probes.

### III.A. Mesh Refinement Study

To assess the necessary grid resolution to resolve flow features and quantities of interest, a grid sensitivity study was conducted for the low speed case. Figures 5a-d present the magnitude of vorticity on a cutting plane passing through the centerline of the hub. This figure shows results from early on in the simulations, when the blades are 250 degrees into the first rotation. A nonlinear color map was chosen to highlight weaker parts of the vorticity field. Based on available resources and this mesh study, all other analysis was conducted using the same mesh as in Figure 5c, where  $\Delta x = 2\text{mm}$  near the blades.

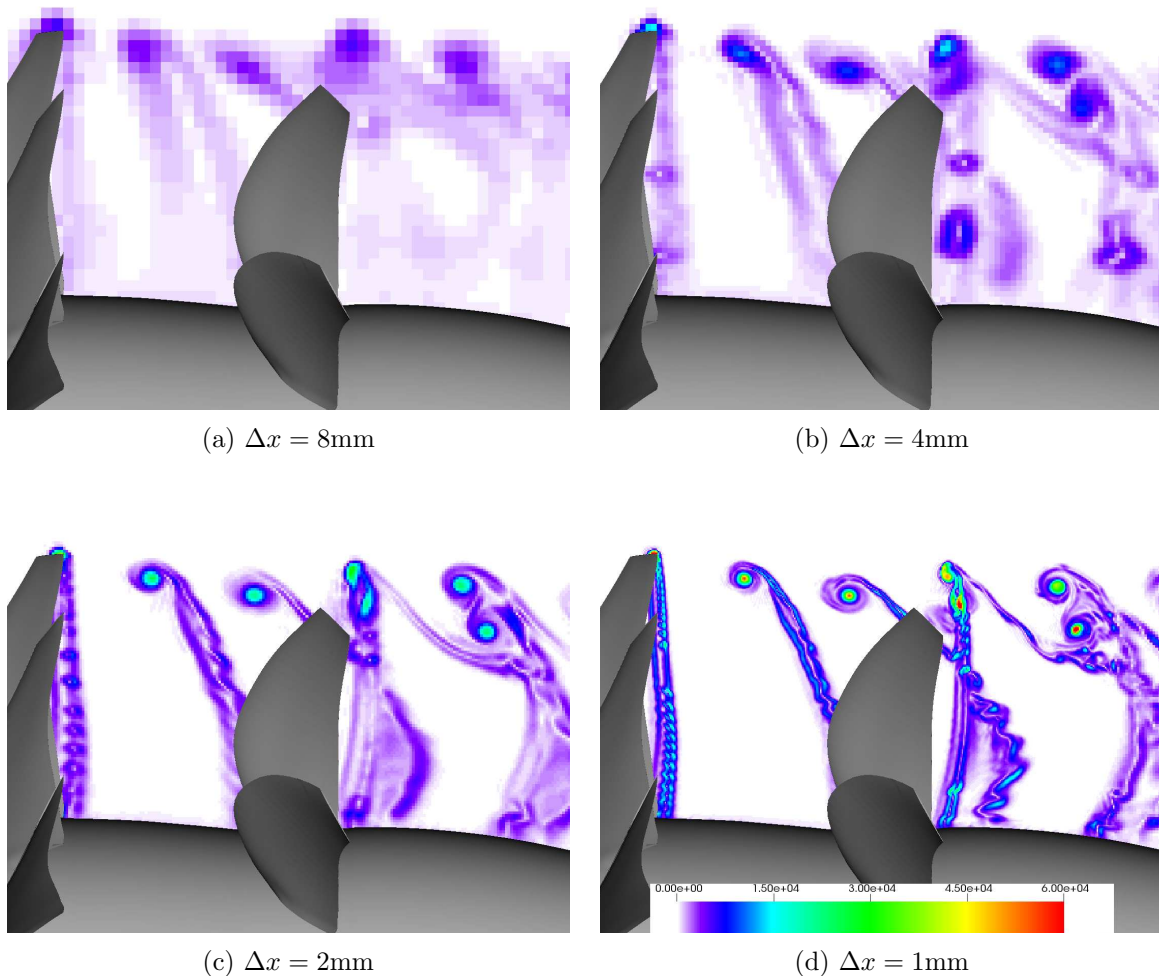
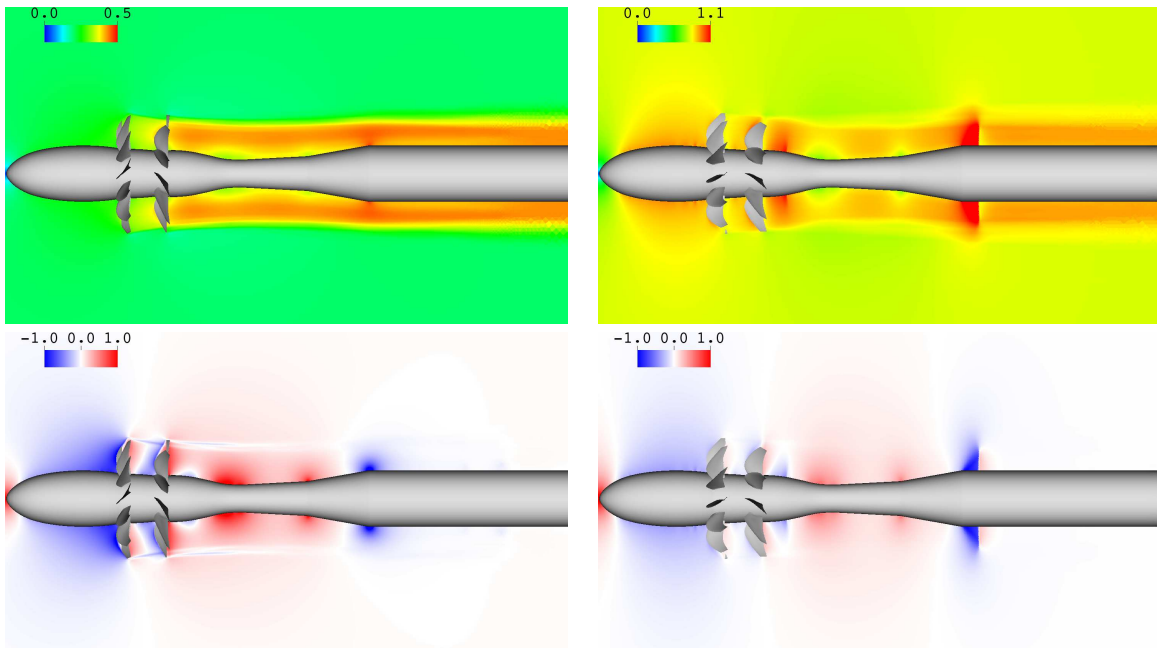


Figure 5. Contours of vorticity magnitude in the center plane for the Mach 0.2 condition, at different mesh refinements in the blade region. These snapshots are all at 250 degrees into the first rotation, during the startup transients.

## IV. Main Flow Features

The time-averaged flow fields are shown in Figures 6a-d in terms of local Mach number and normalized gauge pressure color contours. For both Mach numbers, a local speed-up of the flow can be noted just downstream of the aft rotor blades. For the high speed case, supersonic speeds can be identified around the rotor blades and in some parts of the wake. A fish-tail shock is formed far downstream of the rotor blades where the hub transitions from a narrow to a wider cross-section.



**Figure 6.** Mean flow contours of local Mach number (top) and gauge-pressure (bottom) in the center plane for Mach 0.2 (left) and Mach 0.78 (right).

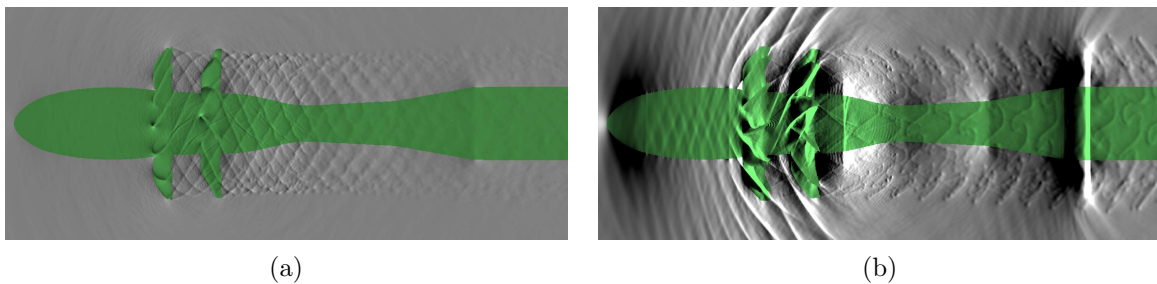


**Figure 7.** Instantaneous Schlieren contours for (a) the low and (b) high speed flow conditions.

Figures 7a-b show instantaneous (numerical) Schlieren contours for the high and low speed flow conditions. A cross-section of the geometry is shown in green. The numerical Schlieren contours were obtained by computing line integrals of the density gradient in the view normal direction through the volume of the instantaneous flow field. The instantaneous flow fields for the low and high speed cases are distinctly different. While the pressure waves that are being generated by the front and rear rotors are almost not visible in the low speed case, strong pressure waves are obtained in the high speed case. The highly unsteady tail shock is clearly highlighted in the Schlieren contours. For the high speed case, the acoustic pressure field is dominated by the dominant acoustic waves thrown off by the front and rear rotors. These distinct pressure waves will generate strong peaks in the frequency spectra at distinct BPFs. In this work, the blade-passing-frequency of the front rotor is referred to as BPF1 and for the rear rotor as BPF2. The tip-vortices emerging from the front of the rotors can also be identified in the Schlieren images. The tip-vortices from the front blade impinge on (or barely grace) the aft rotor blade as well as interact with the tip-vortices of the second rotor. In the wake of the rotors these highly energetic tip-vortices are deformed very differently for the low and high speed cases. A stronger modulation of these vortex tubes can be noted for the high speed case. One of the key challenges for simulating this flow field is to be able to capture the interaction tones as well as broadband noise that is mainly introduced by the finer-scale turbulence motion in the wake. For the low speed conditions, the SPL of the broadband noise component is significantly closer to the tonal noise than in the high speed case. Thus, the low speed case is considerably more challenging requiring an accurate prediction of high-order interactions.

## V. Comparison with Experimental Data

### V.A. Meanflow

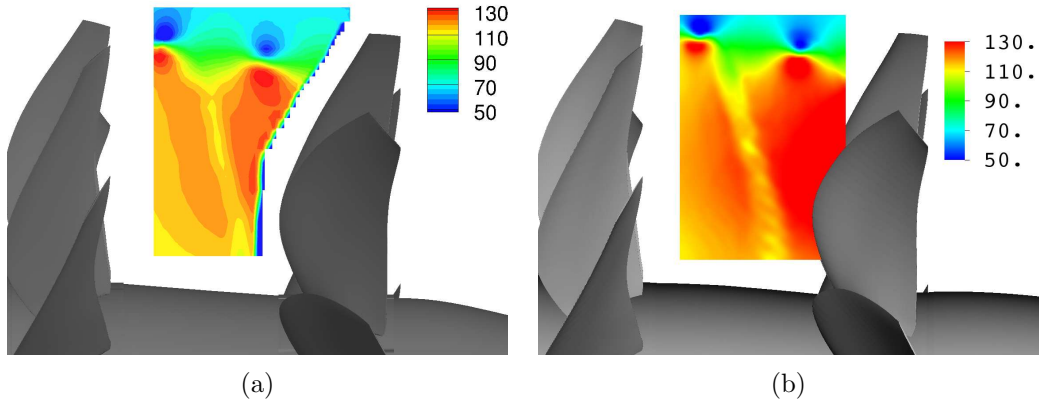


Figure 8. Comparison of (a) experimental PIV results and (b) CFD data considering absolute velocity in the center-plane.

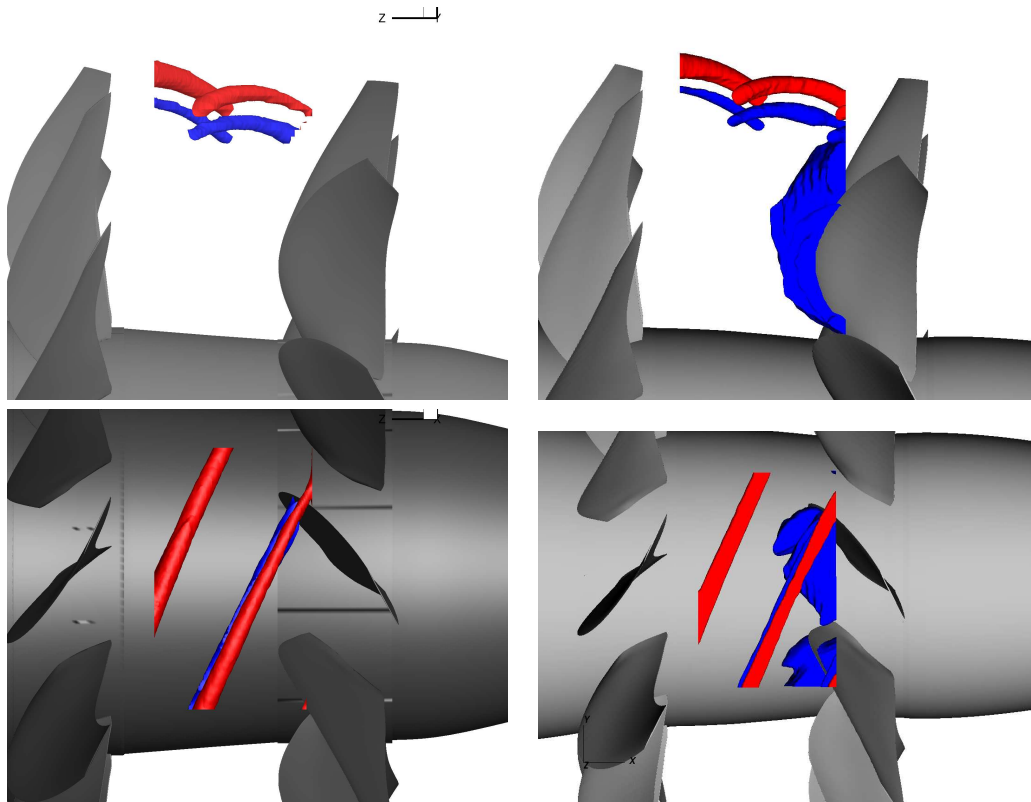


Figure 9. Comparison of (a) experimental PIV results and (b) CFD data considering iso-surfaces of velocity magnitude (bottom) for  $|v|/v_\infty = 0.84$  (red) and  $1.91$  (blue).

In order to capture the correct noise generation mechanisms in the source region it is a requisite to simulate the correct mean flow features. In what follows, the simulation results are compared to PIV data that was made available from the low speed test in NASA's 9-foot  $\times$  15-foot low-speed acoustic wind tunnel. Figures 8a and 8b show a side-by-side comparison of velocity magnitude contours from experimental PIV measurements and the CFD simulation. Although, slightly different post-processing procedures were used the location and strength of the tip vortices are in good agreement with experimental data in the cut-plane. Iso-contours of velocity magnitude with  $|v|/v_\infty = 0.84$  (red) and  $1.91$  (blue) are presented in Figures 9a and

9b. The orientation and size of the tip vortices seem to be well captured with the current simulation setup. This is important in order to capture the blade vortex interaction of the trailing tip vortices from the front rotor blades interacting with the rear rotor.

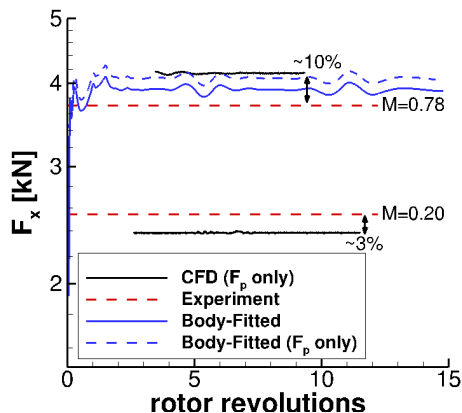


Figure 10. Thrust comparison between low/high speed experiments and CFD simulations.

The thrust coefficient is one of the key parameters for the open rotor design. Thus, next the thrust values extracted from the CFD simulations are compared to the values obtained in the experiments. Figures 10a and 10b show the temporal evolution of the thrust force from the CFD simulations. Note that the thrust value is obtained by a surface integral over the front and rear rotor surfaces only. For the low speed case, the results are within 5% of the experimental data and for the high speed case within 10%. The large discrepancy at this point is due to the fact that only the pressure force is accounted for in the CFD force extraction. The ratio between pressure and viscous forces is roughly 100 to 4 for the high speed case. This value was determined from the overset simulation results with LAVA-Curvilinear by Housman et al.<sup>6</sup> Considering the pressure force only, the difference between thrust values from the experiment and the CFD simulation reduces to a deviation of about 6% for the high speed case. For the low speed case, the thrust is under-predicted but at this point it is not necessarily clear if considering viscous forces would increase or reduce the error because the low speed simulation with LAVA-Curvilinear was not available at the time the paper was prepared.

### V.B. Selection of Acoustic Surfaces

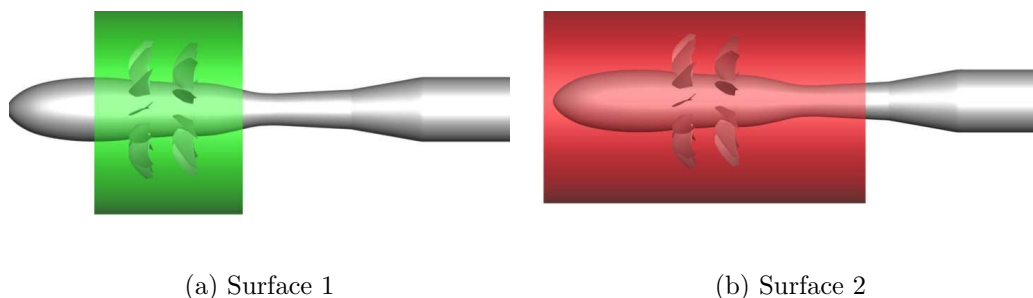


Figure 11. Permeable acoustic surfaces used for propagating acoustic noise signature from the near-field to the Kulite sensors in the far-field.

Since the Kulite sensors are located a considerable distance away from the open rotor system, the FW-H method is employed in this work to propagate the near field acoustic data to the Kulite sensor locations. Figures 11a and 11b display the permeable surfaces used for the FW-H method. Different variations of the permeable surfaces were tested and are referred to as surface 1 in Figure 11a and surface 2 in Figure 11b. Both surfaces consist of a cylindrical shell that is capped off in the front and back with two circular surfaces. It is well-known that the hydrodynamic pressure fluctuations in the wake may pollute the FW-H source data obtained on the circular surface cutting through the wake. In order to study this effect, an

additional variation of these acoustic surfaces was created by removing the circular surfaces cutting through the wake. These surfaces are subsequently referred to as “surface 1/2 (open)”.

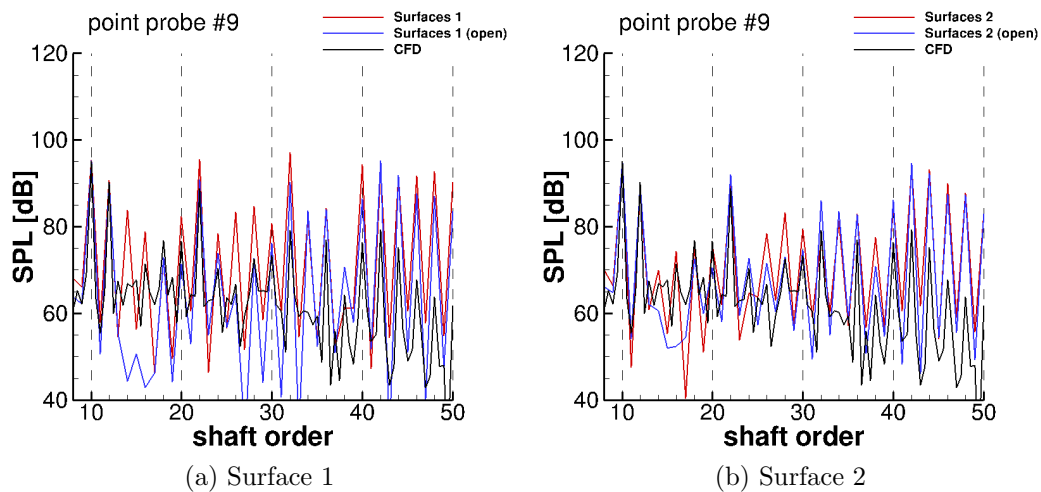


Figure 12. SPL spectra at Kulite sensor #9 for the two different acoustic surfaces (surfaces 1 and 2) and acoustic data directly extracted from the low speed CFD simulations.

Figures 12a and 12b present different Sound Pressure Level (SPL) spectra at Kulite #9 for the FW-H method considering different acoustic surfaces, and the SPL spectra directly computed from the CFD simulation of the low speed case. By comparing the different spectra an appropriate permeable surface is selected that can be used to obtain spectra for Kulite sensors that are located much further away from the source region. On the coarse mesh, the grid resolution is sufficient to resolve acoustic waves up to a shaft order of roughly 40 with 8 points per wavelength (PPW). Hence, beyond a shaft order of 40 a significant reduction in SPL can be noted in the spectra extracted from the CFD simulation. The strong reduction in the wave amplitudes can be attributed to substantial numerical dissipation for large wavenumbers. Removing the surface cutting through the wake greatly affects the peaks that can be observed in the spectra. For surface 1, some spurious tones can clearly be identified. When increasing the size of the sampling surface the differences in the spectra between surface 02 and surface 02 (open) are much smaller. The results for surface 02 are slightly closer to the CFD data than the results for surface 01. Hence, from this point forward all spectra were computed considering surface 02 (open).

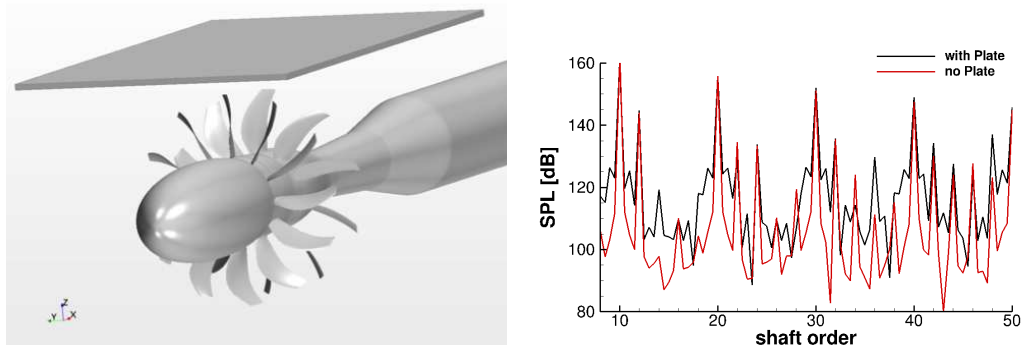


Figure 13. (a) Open rotor geometry and large plate with embedded pressure sensors. (b) SPL plots from CFD simulation at sensor #9 with and without plate.

In the high speed experimental tests the Kulite pressure sensors were embedded into large plate as shown in Figure 13a. Note that the plate was only used in the smaller wind tunnel for the high speed tests. Throughout the paper the effect of the plate was considered by accounting for the wave reflection on the solid wall by subtracting 6dB ( $=10\log_{10}(2^2)$ ) from the measured data. The additional effects of the plate on the acoustic data was tested in the CFD simulation. In the simulation with plate, the plate was placed at the height of the first row of Kulite sensors with  $h = 0.43\text{m}$ . A significant effect on the broadband noise signature can be observed. The tonal peaks, however, seem to be only mildly affected by the presence of

the plate. Considering that in the high speed tests the overall sound pressure level (OASPL) is dominated by tonal noise the CFD results confirm that the additional plate effects can be neglected for the further discussion of the results.

### V.C. Comparison of Far-Field Acoustic Data

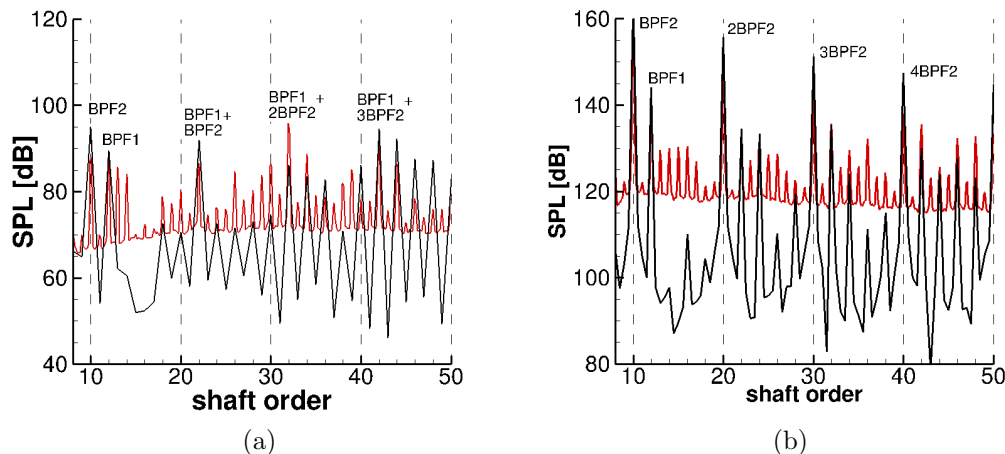


Figure 14. Sound pressure level (SPL) spectra for (a) the low speed and (b) high flow speed conditions at Kulite #9. Experimental data is shown with red lines and coarse grid computations with black lines.

A comparison of the far-field acoustic spectra between CFD and experimental data is provided in Figures 14a and 14b. For both the low and high speed experiments the spectra are compared at Kulite sensor #9. It should be pointed out that although the sensor numbers are identical the actual physical locations are different with vertical distances to the rotor axis of  $h = 1.53\text{m}$  and  $h = 0.43\text{m}$  for the low and high speed cases, respectively. An important difference between the SPL spectra for the low and high speed tests is that the broadband noise level is much closer to the tonal peaks for the Mach 0.2 flow conditions. This makes the low speed case more difficult to simulate. It is important to provide sufficient grid resolution to capture some of the higher-order interactions. Due to insufficient grid resolution the large tip vortices may not break up as quickly and, therefore, some of the distinct tones are slightly over-predicted in the spectra. This result is consistent with the observations for the high speed case by Housman *et al.*<sup>6</sup> utilizing a conventional overset approach to simulate the flow around the open rotor. Overall, the tonal peaks compare well with spectra obtained in the experiment. Quantitatively the harmonics of the front ( $m \times \text{BPF1}$ ) and the rear ( $n \times \text{BPF2}$ ) rotors are within a range of  $\pm 1 - 2\text{dB}$  and the interaction tones are within a range of  $\pm 5\text{dB}$  to the experimental data. Finer grid resolution is needed to capture the higher-order interaction tones ( $m \times \text{BPF1} + n \times \text{BPF2}$ ) more accurately.

The dependence of SPL on the geometric angle for first-order and higher-order interaction tones is displayed in Figures 15a and 15b. Note that in the experimental data the shaft orders were not matched exactly so that the tones are obtained by a logarithmic sum including the neighboring samples. The CFD data matches the general trends and amplitudes from the experimental results well except for an outlier at roughly  $130^\circ$ . It was expected that the results for the last Kulite sensors may be less accurate due to a significant reduction in grid resolution in the wake. The SPL values for the first-order tones are significantly higher around the location of the rotor blades. The acoustic wave amplitudes associated with BPF2 are slightly higher than for BPF1. To ease the comparison in Figure 15b for the higher-order interaction tones some of the spectra were shifted by  $\pm 20\text{dB}$  because all of the higher-order interaction tones shown here contain similar SPL values. It appears that also the higher-order interactions are captured well with the current simulation approach. The OASPL between a geometric angle of  $70^\circ - 120^\circ$  is dominated by the contributions from the first-order tones, i.e., BPF1 and BPF2. Interestingly, away from the center (at  $90^\circ$  geometric angle) the contributions from higher harmonics of the fundamental tones and higher-order interaction tones become increasingly more relevant. In addition, the OASPL does not peak in the center but it increases with increasing observer angles. This happens although the first-order tones decay rapidly with increasing geometric angle. These results confirm that in order to correctly predict the OASPL for the low flow speed

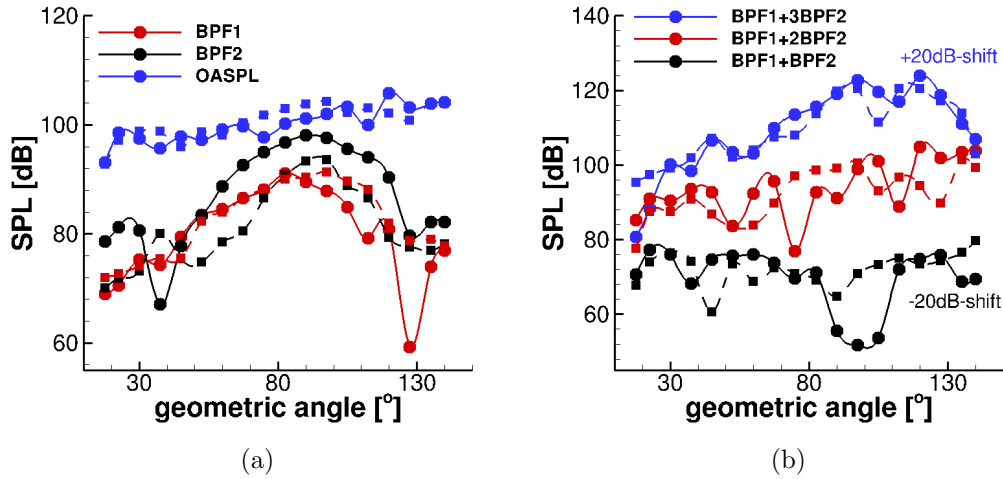


Figure 15. Dependence of SPL on the geometric angle for (a) first-order and (b) higher order interaction tones. The solid and dashed lines with circular and squared symbols mark the CFD and experimental data for the low speed case, respectively.

case the higher harmonics and higher-order interaction tones need to be correctly predicted.

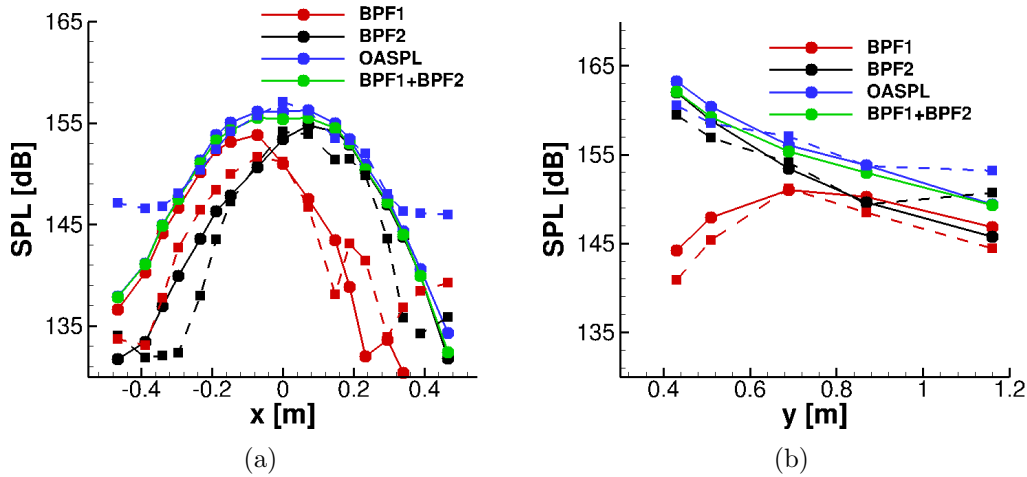


Figure 16. Variation of SPL in (a) x-direction with  $y = 0.53\text{m}$  and (b) y-direction starting at Kulite #9 for the high speed flow conditions. The solid and dashed lines with circular and squared symbols mark the CFD and experimental data, respectively.

In the high speed experiment, the Kulite sensors were distributed horizontally and vertically. The variation of SPL in horizontal direction with  $y = 0.53\text{m}$  (Kulite sensors 18 to 34) is compared between the CFD and experimental results in Figure 16a. The SPLs for BPF1 and BPF2 as well as the OASPL from the CFD simulations are in close agreement with the experimental data. In contrast to the low speed data, the OASPL is dominated almost over the entire x-range by the first-order tones generated by the front and rear rotors. The OASPL peaks around  $x = 0\text{m}$  and decays rapidly away from the center of the rotors. For comparison purposes the OASPL only considering BPF1 and BPF2 was added in Figures 16a and 16b.

The variation of SPL in vertical direction (starting at Kulite sensor #9) is compared between the CFD and experimental results in Figure 16b. The general trend and amplitude levels are in good agreement between the results from the experiment and CFD. Only a small deviation between data from the experiments and CFD is observed for  $y = 1.2\text{m}$ . While the SPL for BPF1 strictly reduces in y-direction the SPL for BPF2 peaks at around  $y = 0.8\text{m}$ . The initial increase in SPL for BPF1 is due to the fact that the source regions for the BPF1 and BPF2 tones are spatially separated. Each of the tones in the spectra contains a unique directivity pattern of its associated acoustic waves. The comparison of the experimental and CFD data provide great confidence that the current CFD simulations are able to capture the main noise generation mechanisms. In the following Section VI, the CFD results are further analyzed to provide some insight about

the noise generation in the source region and the acoustic wave propagation pattern in the near-field.

## VI. Near-Field Acoustic Analysis

While the main focus of this paper is on validating the immersed boundary approach for computational aero-acoustic (CAA) predictions of the open rotor system, the current section provides a brief overview of the acoustic near-field. One of the key objectives for developing this high-fidelity CAA simulation capability is that a wealth of information becomes available that can be used for improving the understanding of the noise generation mechanisms in the open rotor system.

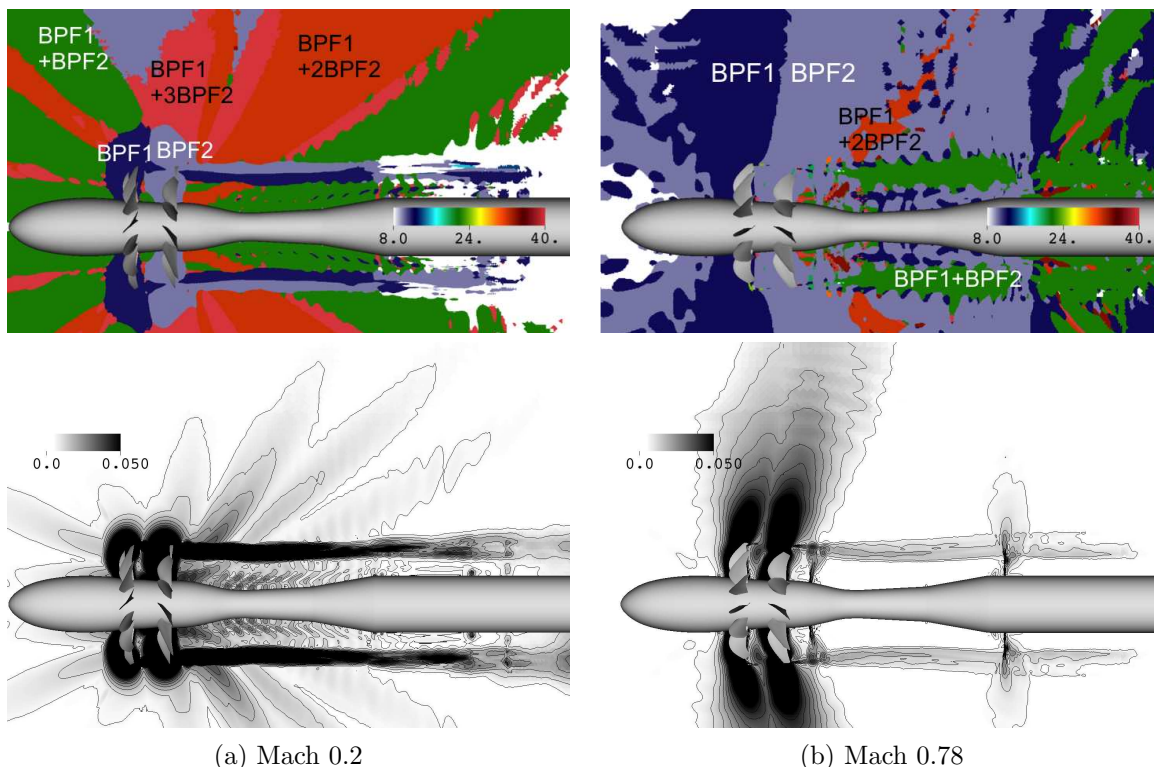
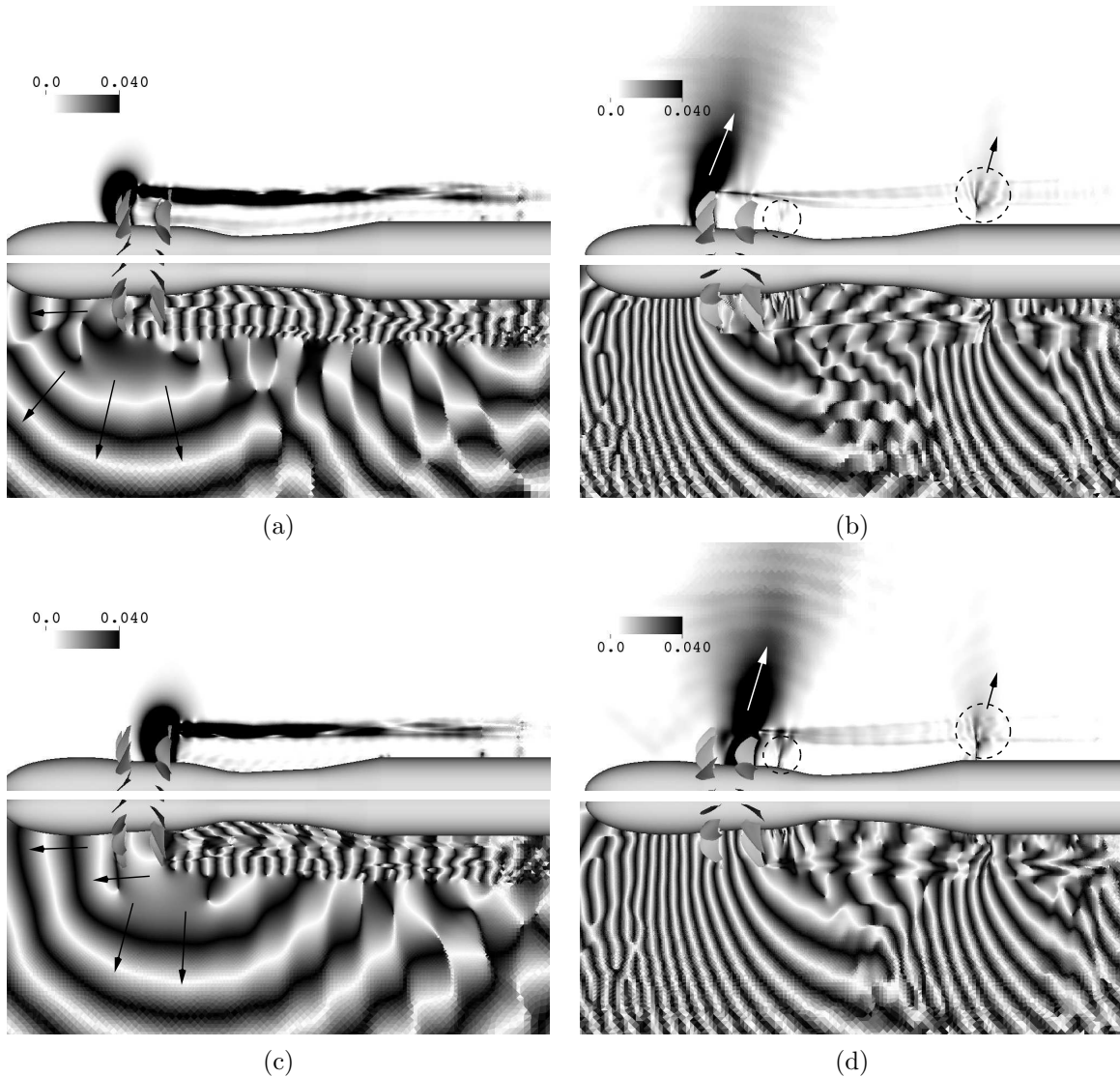


Figure 17. Most dominant frequencies (in BPF) and corresponding Fourier amplitude displayed in the center-plane cutting through the open rotor.

Figures 17a and 17b show the most dominant frequencies (top) and its amplitudes (bottom) in the center-plane of the open rotor for the low and high speed flow conditions. When analyzing the results it is important to keep in mind that the dominant frequencies in the center-plane are not only associated with acoustic but also entropy and vorticity waves are present. The difference in phase speeds becomes obvious in the phase plots where the associated wavelengths can be identified. As it has been pointed out above, the acoustic noise field is very different for the low and high speed cases. For the high speed case, the most dominant pressure waves right in front of the open rotor are associated with the front rotor BPF1 while the rear rotor BPF2 remains dominant over a large region starting right behind the front rotor. In the low speed case, the regions where BPF1 and BPF2 are the most dominant tones are significantly smaller and constrained to a small region around the front and rear rotors extending from the tips of the rotors into the free-stream. The interaction tone BPF1+BPF2 is the most dominant tone for the high speed case in the wake where the tip vortices from the front and rear rotors interact with each other. While the inner wake region (towards the rotor axis) is mainly dominated by BPF2 (with some patches of BPF1) for the high speed case, the interaction tone BPF1+BPF2 is most dominant for the low speed case. For the high speed case, a large extent of the cut-plane is dominated by the first-order tones of the front and rear rotor except for a small region downstream of the rear rotors right above the wake where a higher-order interaction tone (BPF1+2×BPF2) becomes dominant. In addition, downstream of the unsteady tail shocks the interaction tone BPF1+BPF2 takes over. A possible explanation for this is that the trailing vortices that interact which each other drive the unsteady motion of the shock. For the low speed case, different higher-order interaction

tones are dominant in the cut plane. The sources for these pressure waves and their wave propagation patterns are analyzed by considering spectral amplitude and phase plots for the different tones.



**Figure 18. Amplitude (top) and phase (bottom) distributions for first-order tones associated with the front and rear rotors: (a) BPF1 for low speed case, (b) BPF1 for high speed case, (c) BPF2 for low speed case, and (d) BPF2 for high speed case.**

The amplitude distribution for BPF1 and BPF2 in Figures 18a-d display large values around the front and rear rotors, respectively. The vortices emerging from the tip of the front and rear rotors remain dominant in the wake and an interaction with the tail shock can be noted. For the high speed case the amplitude is, however, significantly lower than for the low speed case. From the flow visualization, the tip vortices seem to interact more strongly with each other in the high speed case. The wake that is still dominated by the strong tip vortices and their interactions seem to induce the dominant motion of the tail shock which is indicated by the large amplitudes for BPF1 and BPF2 in this region. Another weaker shock is formed right behind the rear rotor. The motion of this shock is dictated by the unsteadiness in the near wake right behind the rear rotor, thus, BPF2 is the dominant frequency in this region.

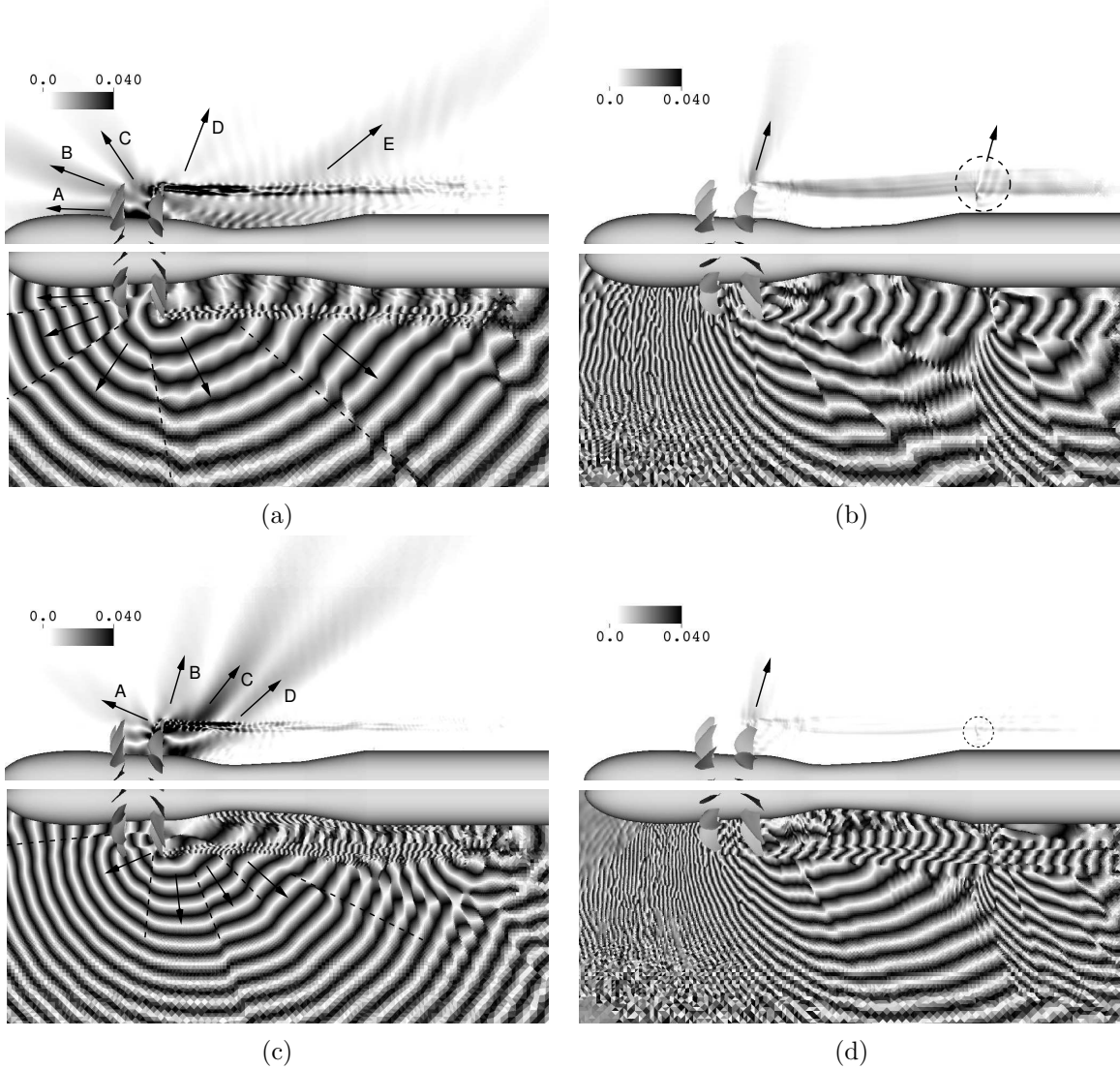


Figure 19. Amplitude (top) and phase (bottom) distributions for higher-order interaction tones: (a)  $BPF1+BPF2$  for low speed case, (b)  $BPF1+BPF2$  for high speed case, (c)  $BPF1+2\times BPF2$  for low speed case and (d)  $BPF1+2\times BPF2$  for high speed case.

The amplitude and phase plots for the higher-order interaction tones are shown in Figures 19a and 19b. For the high speed case, large amplitudes for  $BPF1+BPF2$  emerge from the top of the rear rotor. The interaction of the rear rotor with the tip vortex from the front rotor can be made responsible for the generation of these pressure waves. A similar interaction can be observed for the low speed case while for the lower free-stream Mach number the pressure waves are able to propagate upstream. The large tonal amplitudes for  $BPF1+BPF2$  at the tip vortices in the wake of the rotors was previously pointed out for the high speed case and can be attributed to the interaction of the tip vortices from the forward and rear rotors. When comparing the amplitude distributions for the higher-order interaction tones it becomes obvious that the higher-order interactions play a more critical role for the prediction of the OASPL in the low speed case than in the high speed case. Two additional regions with large amplitudes for  $BPF1+BPF2$  can be identified for the low speed case. The first region marked with “C” appears to originate from the midsection of the aft rotor. These pressure waves may be generated by the aft rotor cutting through the unsteady wake of the front rotor. These pressure waves are not observed for the high speed case because the flow is supersonic in the region between the two rotors. The second region with large amplitudes of  $BPF1+BPF2$  (marked with “E”) originates from the large wake behind the rotor system. Similar interactions can be observed for  $BPF1+2\times BPF2$ . The interactions of the rear rotor with the tip vortex from the front rotor is the only

mechanism that is highlighted for the high speed case. For the low speed case, region “A” and “B” and possibly even region “C” are related to a similar blade-vortex-interaction (BVI) mechanism of the rear rotor with the tip vortex from the front rotor. Note that the diameter of the rear rotor is slightly smaller than the diameter of the front rotor to reduce BVI. It is difficult to fully eliminate the interaction for a practical design where a reasonable thrust coefficient must be obtained. Another higher-order interaction region is marked with “D” and originates from the inner wake right behind the rear rotor. Some of the distinct wave fronts that appear in the phase plots can clearly be associated with the regions marked in amplitude plots.

## VII. Summary and Outlook

In the present paper, a higher-order accurate immersed boundary method was employed to simulate the flow field around a contra-rotating open rotor. Two experiments, the Mach 0.2 experiment conducted in NASA’s 9-foot  $\times$  15-foot low-speed acoustic wind tunnel and the Mach 0.78 experiment conducted in NASA’s 8-foot  $\times$  6-foot wind tunnel, were simulated. Some of the key challenges for employing the immersed boundary method for this setup, such as the treatment of the very thin rotor blades, moving boundaries, and viscous wall effects, were successfully addressed. The current simulation strategy was validated by comparing the simulation results with available experimental data. Good agreement between PIV measurements and the CFD simulations of the flow field between the front and rear rotors was obtained. The immersed boundary simulations are also in close agreement with other more conventional CFD approaches, such as LAVA-Curvilinear.<sup>6</sup> It appears that with the current simulation strategy it is possible to correctly capture some of the key flow features, such as strength and orientation of the tip vortices from the rotors.

In addition, Kulite pressure sensor data recorded in the two experiments was compared to the simulation data. In order to obtain the acoustic pressure field at the far-field locations the unsteady flow data was recorded on carefully selected permeable surfaces and the Ffowcs-Williams Hawkings method was employed for the acoustic far-field propagation. The comparison of the acoustic measurements with the CAA results show close agreement to each other for single tones as well as the OASPL at the different pressure sensors. As it has been pointed out by other researchers, the prediction of the higher-order interaction tones is computationally more demanding than predicting the single harmonic tones of the front and rear rotors. Since the OASPL for the high speed case is dominated by the BPF1 and BPF2 tones it appears that the low speed case is computationally more challenging where the interaction tones play a more dominant role. Moreover, the magnitude of the broadband sound, mainly generated in the wake, is much closer to the isolated tones for the low speed case. In order to capture the broadband noise generation mechanisms correctly a highly accurate solution is needed to capture the main features of the turbulent wake. Therefore, higher-order schemes are desirable in order to provide an efficient simulation capability for these flow fields.

Finally, the simulation data was utilized to provide some insight about the noise generation mechanisms of the contra-rotating open rotor. Important differences between the acoustic noise field for the low and high speed cases were pointed out. In the high speed case, the OASPL peaks around 90° geometric angle and decays rapidly away from the center. In the low speed case, the OASPL keeps increasing towards larger geometric angles until the end of the recorded interval at around 150°. The main explanation for not obtaining a local peak in the OASPL within the measured range is that while in the high speed case the noise is mostly generated by the BPF1 and BPF2 tones, in the low speed case higher-order interactions play a much more dominant role. For the low speed case, noise generation through blade vortex interaction and in the inner wake appear to be much more relevant for the OASPL.

In summary, it was demonstrated that LAVA’s higher-order immersed boundary method is capable of predicting the acoustic noise field around the contra-rotating open rotor for the nominally take-off and cruise conditions. Recent publications by Envia<sup>5</sup> and others have demonstrated that specific turbo-machinery tools provide the capability of predicting isolated performance of the contra-rotating open rotor that includes aero-acoustic predictions as well. Currently, there exists great interest in the prediction of installation effects. Due to the assumptions that were made in the development of these specific turbo-machinery tools it is, however, difficult or even impossible to apply them to complex integrated airframe-propulsion systems. Hence, the next step of this research is to leverage the present simulation capability to study installation effects. The key advantage of the current approach is that complex geometries can be simulated without going through the time-consuming grid generation process. Furthermore, efficient higher-order methods can be employed on Cartesian meshes with adaptive mesh refinement. A high-fidelity LAVA simulation of a fully installed open-rotor system with the current strategy can be used to obtain an improved understanding of the noise

generation process. Nevertheless, this approach still requires a significant amount of computational resources due to the wide range of relevant scales that are involved in the noise generation process. For design purposes, however, a rapid analysis capability is desirable. Thus, in order to obtain a rapid analysis capability the higher-order immersed boundary approach may only be used to capture the relevant aerodynamic features such that the acoustic noise characteristics can be efficiently predicted by utilizing an acoustic analogy.

## References

- <sup>1</sup>Spalart, P., Travin, A., Shur, M., and Strelets, M., "Initial Noise Predictions for Open Rotors Using First Principles," *16th AIAA/CEAS Aeroacoustics Conference, Stockholm, Sweden*, June 2010, AIAA-2010-3793.
- <sup>2</sup>Rebecca Busch, E., Kebler, M., and Kramer, E., "Aeroacoustics of a High-Fidelity CFD Calculation of a Counter-Rotating Open Rotor in Take-Off Conditions," *19th AIAA/CEAS Aeroacoustics Conference, Berlin, Germany*, May 2013, AIAA-2013-2202.
- <sup>3</sup>Ben Nasr, N., Ortun, B., Chelius, A., and Canard-Caruana, S., "Assessment of advanced grid strategies for CFD on open rotor applications," *49th AIAA/ASME/SAE/ASEE Joint Propulsion Conference, San Jose, CA*, July 2013, AIAA-2013-3800.
- <sup>4</sup>Node-Langlois, T., Wlassow, F., Languille, V., Colin, Y., Caruelle, B., Gill, J., Chen, X., Zhang, X., and Parry, A., "Prediction of Contra-Rotating Open Rotor Broadband Noise in Isolated and Installed Configurations," *20th AIAA/CEAS Aeroacoustics Conference, Atlanta, Georgia*, June 2014, AIAA-2014-2610.
- <sup>5</sup>Envia, E., "Contra-Rotating Open Rotor Tone Noise Prediction," *20th AIAA/CEAS Aeroacoustics Conference, Atlanta, Georgia*, June 2014, AIAA-2014-2606.
- <sup>6</sup>Housman, J. and Kiris, C., "Structured Overlapping Grid Simulations of Contra-Rotating Open Rotor Noise," *54th AIAA Aerospace Sciences Meeting, San Diego, CA*, 2016.
- <sup>7</sup>Peskin, C., "Numerical Analysis of Blood Flow in the Heart," *J. Comput. Phys.*, Vol. 25, 1977, pp. 220–252.
- <sup>8</sup>Peskin, C. S., "The Immersed Boundary Method," *Acta Numerica, Cambridge University Press*, 2002, pp. 1–39.
- <sup>9</sup>Goldstein, D., Handler, R., and Sirovich, L., "Modeling a Non-Slip Flow Boundary with an External Force Field," *J. Comp. Phys.*, Vol. 105, 1993, pp. 354–366.
- <sup>10</sup>LeVeque, R. J., *Time-Split Methods for Partial Differential Equations*, Ph.D. thesis, Stanford University, 1982.
- <sup>11</sup>Wiegmann, A. and Bube, K., "The Explicit–Jump Immersed Interface Method: Finite Difference Methods for PDEs with Piecewise Smooth Solutions," *SIAM J. Numer. Anal.*, Vol. 31(4), 1992, pp. 1019–1044.
- <sup>12</sup>Linnick, M. and Fasel, H., "A High–Order Immersed Interface Method for Simulating Unsteady Incompressible Flows on Irregular Domains," *J. Comput. Phys.*, Vol. 204, 2004, pp. 157–192.
- <sup>13</sup>Johansen, H. and Colella, P., "A Cartesian Grid Embedded Boundary Method for Poisson’s Equation on Irregular Domains," *Journal of Computational Physics*, Vol. 147, 1998, pp. 60–85.
- <sup>14</sup>Mittal, R. and Iaccarino, G., "Immersed Boundary Methods," *Annu. Rev. Fluid Mech.*, Vol. 37, 2005, pp. 239–261.
- <sup>15</sup>Zhong, X., "A New High–Order Immersed Interface Method for Solving Elliptic Equations with Embedded Interface of Discontinuity," *Journal of Computational Physics*, Vol. 225, 2007, pp. 1066–1099.
- <sup>16</sup>Duan, L., Wang, X., and Zhong, X., "A High–Order Cut–Cell Method for Numerical Simulation of Hypersonic Boundary–Layer Instability with Surface Roughness," *Journal of Computational Physics*, Vol. 229, 2010, pp. 7207–7237.
- <sup>17</sup>Kiris, C., Barad, M., Housman, J., Sozer, E., Brehm, C., and Moini-Yekta, S., "The LAVA Computational Fluid Dynamics Solver," *52st AIAA Aerospace Sciences Meeting, National Harbor, Maryland*, January 13-17, 2014, AIAA-2014-0070.
- <sup>18</sup>Nemec, M. and Aftosmis, M., "Aerodynamic Shape Optimization Using a Cartesian Adjoint Method and CAD Geometry," *24th AIAA Applied Aerodynamics Conference, AIAA 2006-3456*, 2006.
- <sup>19</sup>Mittal, R., Dong, H., Bozkurttas, M., Najjar, F., Vargas, A., and von Loebbecke, A., "A Versatile Sharp Interface Immersed Boundary Method for Incompressible Flows with Complex Boundaries," *Journal of Computational Physics*, Vol. 227, 2008, pp. 4825–4852.
- <sup>20</sup>Brehm, C. and Fasel, H., "A Novel Concept for the Design of Immersed Interface Methods," *Journal of Computational Physics*, Vol. 242, No. 0, 2013, pp. 234 – 267.
- <sup>21</sup>Brehm, C., Hader, C., and Fasel, H., "A Locally Stabilized Immersed Boundary Method for the Compressible Navier-Stokes Equations," *Journal of Computational Physics*, Vol. 295, 2015, pp. 475–504.
- <sup>22</sup>Berger, M. J. and Colella, P., "Local Adaptive Mesh Refinement for Shock Hydrodynamics," *J. Comput. Phys.*, Vol. 82, No. 1, May 1989, pp. 64–84.
- <sup>23</sup>Almgren, A. S., Bell, J. B., Colella, P., Howell, L. H., and Welcome, M. L., "A Conservative Adaptive Projection Method for the Variable Density Incompressible Navier-Stokes Equations," *J. Comp. Phys.*, Vol. 142, 1998, pp. 1–46.
- <sup>24</sup>Barad, M. F. and Colella, P., "A Fourth-Order Accurate Local Refinement Method for Poisson’s Equation," *J. Comp. Phys.*, Vol. 209, No. 1, October 2005, pp. 1–18.
- <sup>25</sup>Barad, M. F., Colella, P., and Schladow, S. G., "An Adaptive Cut-Cell Method for Environmental Fluid Mechanics," *Int. J. Numer. Meth. Fluids*, Vol. 60, No. 5, 2009, pp. 473–514.
- <sup>26</sup>Zhang, Q., Johansen, H., and Colella, P., "A Fourth-Order Accurate Finite-Volume Method with Structured Adaptive Mesh Refinement for Solving the Advection-Diffusion Equation," *SIAM Journal on Scientific Computing*, Vol. 34, No. 2, 2012, pp. 179–201.
- <sup>27</sup>Colella, P., Graves, D. T., Ligocki, T. J., Martin, D. F., Modiano, D., Serafini, D. B., and Straalen, B. V., "Chombo Software Package for AMR Applications - Design Document," unpublished.
- <sup>28</sup>Brehm, C., Housman, J., and Kiris, C., "Noise Generation Mechanisms for a Supersonic Jet Impinging on an Inclined Plate," *J. Fluid Mech.*, ~2015, submitted in March 2015.

<sup>29</sup>Brehm, C., Housman, J., Kiris, C., and Hutcheson, F., “Noise Characteristics of a Four-Jet Impingement Device Inside a Broadband Engine Noise Simulator,” *21st AIAA/CEAS Aeroacoustics Conference, Dallas, TX*, 2015, AIAA 2015-2211.

<sup>30</sup>van Leer, B., “Flux Splitting for the Euler Equations,” *International Conference on Numerical Methods in Fluid Dynamics*, Vol. 170, 1982, pp. 507–512.

<sup>31</sup>Brehm, C., Barad, M., and Kiris, C., “An Immersed Boundary Method for Solving the Compressible Navier-Stokes Equations with Fluid-Structure Interaction,” *54th AIAA Aerospace Sciences Meeting, San Diego, CA*, 2016.

<sup>32</sup>Brehm, C., Barad, M., and Kiris, C., “Towards a Viscous Wall Model for Immersed Boundary Methods,” *AIAA Aviation and Aeronautics Forum and Exposition, Washington, DC*, 2016.